HHS Public Access

Author manuscript

Ocul Surf. Author manuscript; available in PMC 2023 April 01.

Published in final edited form as:

Ocul Surf. 2022 April ; 24: 34–39. doi:10.1016/j.jtos.2021.12.011.

Characterization of the Thickness of the Tear Film Lipid Layer in Meibomian Gland Dysfunction using High Resolution Optical Microscopy

Yuqiang Bai[1], **William Ngo**[2,3], **Safal Khanal**[1], **Jason J. Nichols**[1,††]

[1]Department of Optometry and Vision Science, School of Optometry, University of Alabama at Birmingham, Birmingham, AL, USA

[2]Centre for Ocular Research & Education, School of Optometry & Vision Science, University of Waterloo, Waterloo, Ontario, Canada

[3]Centre for Eye and Vision Research (CEVR), 17W Hong Kong Science Park, Hong Kong

Abstract

Purpose.—To evaluate the thickness of the tear film lipid layer (TFLL) in meibomian gland dysfunction (MGD) using a high-resolution optical microscope.

Methods.—The Ocular Surface Disease Index (OSDI) and meibum grade score (MGS) were used to classify 190 subjects into four groups: normal (OSDI<13 and MGS<10), mixed (OSDI≥13 and MGS<10), asymptomatic MGD (OSDI<13 and MGS≥10), and MGD (OSDI≥13 and MGS≥10). The high-resolution optical microscope was used to capture TFLL images *in vivo*. The histograms of TFLL thickness were analyzed and curve-fitted using probability density functions (PDFs).

Results.—There were three obvious peaks in the distributions of TFLL across the groups. From the curve-fitting process, the main outcomes are displayed according to each Gaussian function with the position of peak (μ) and the summed percentage within the range of standard deviation (σ). The normal group had distribution as follows: 33.3 ± 0.005 nm, 26%; 53.9 ± 0.019 nm, 40%; 79.4 ± 0.064 nm, 12%. The mixed group had a distribution as follows: 33.8 ± 0.004 nm, 32%; 53.1 ± 0.115 nm, 21%; 71.7 ± 0.232 nm, 27%. The asymptomatic MGD group had a distribution as follows: 33.5 ± 0.004 nm, 20%; 49.2 ± 0.041 nm, 25%; 62.9 ± 0.063 nm, 47%. The MGD group had a distribution as follows: 34.3 ± 0.004 nm, 34%; 53.7 ± 0.022 nm, 28%; 74.9 ± 0.060 nm, 16%.

Conclusions.—The MGD and mixed groups had the largest percentages of TFLL thicknesses fall within the thinnest modes (peak 34.3 and 33.8 nm, respectively). These data show that measures of central tendency (e.g., averages, medians) do not fully appreciate the variable distributions of TFLL across disease spectra.

††Corresponding author: Jason J. Nichols, The University of Alabama at Birmingham, 1716 University Blvd, Birmingham, AL, 35233.

Keywords

meibomian gland dysfunction; optical microscope; tear film; lipid layer; evaporative dry eye disease

1 Introduction

The precorneal tear film is approximately 3–5 μm thick [1, 2] and is composed of an aqueous-mucin gel phase and an anterior, superficial lipid layer (~ 40–100 nm) [3–6]. The tear film lipid layer (TFLL) is primarily composed of lipids secreted by the meibomian glands (MGs) and primarily includes a mix of non-polar (e.g., cholesterol, cholesteryl ester, wax ester) and polar (e.g., omega-acyl hydroxy fatty acids (OAHFAs), phospholipids) lipids [7–10]. The amphiphilic polar lipids act as a surfactant and allow the hydrophilic aqueous phase to interface with the non-polar lipids or may serve as an evaporative barrier themselves [11–15]. The role of the TFLL is to retard aqueous evaporation and reduce the surface tension of the tear film, allowing it to spread evenly [16–21].

In meibomian gland dysfunction (MGD), the meibomian gland orifices become progressively keratinized, in addition to a loss of meibocyte progenitor cells, leading MG atrophy over time. The resultant narrowing and obstruction of the MG orifices leads to an alteration in the quality and quantity of the secreted lipids [22–24]. Due to insufficient or poor quality lipids supplying the TFLL, the tear film destabilizes rapidly resulting in rapid evaporation of the tear film aqueous, which is the core mechanism driving evaporative dry eye disease [10, 19, 25, 26]. Conventional wisdom has suggested that a thicker TFLL confers greater stability and resistance to evaporation than a thin TFLL [27, 28]. However, this has not been reported consistently and several studies have noted that TFLL thickness alone is not a substantial barrier to aqueous evaporation [19, 20, 29–32].

While tear film thinning is largely driven by aqueous evaporative loss [16, 33], the relation between tear film thinning and TFLL thickness is less clear [20, 27, 34]. One study found that the variability in tear film thinning rates was not fully explained by TFLL thickness and proposed that other factors such as lipid structure and composition could also influence thinning rates [16]. Supporting these notions, other studies found that despite having a thick TFLL, “holes” in the structure of the TFLL could occur and locally destabilize the tear film [32, 35], suggesting that TFLL integrity is independent of thickness. Other studies identified specific OAHFAs or wax esters that retarded evaporation rates [11, 34], providing evidence that lipid composition of the TFLL influences evaporation [26]. Finally, a recent study found that thick TFLLs were associated with greater dry eye symptoms and reduced tear stability [36], highlighting the complex relationship between TFLL thickness and overall tear film health.

Evaporative loss of the tear film is a core element of the pathophysiology of MGD. Addressing knowledge gaps related to TFLL structure could advance the understanding of the pathological tear film in MGD. The purpose of this study was to investigate TFLL thickness and variability across a cohort of subjects with and without MGD using a high resolution, microscopy-based, non-invasive imaging system.

2 Materials and Methods

2.1 Human Subjects

The study adhered to the principles of the Declaration of Helsinki and ethics approval was obtained from the Institutional Review Board at the University of Alabama at Birmingham. A total of 190 human subjects were consented from the University of Alabama at Birmingham Academic Medical Center and the University of Alabama at Birmingham Ocular Surface Research Center IRB approved patient database. Subgroup classifications were determined subsequent to the clinical examination based on the recommendations of the Tear Film and Ocular Surface Society International Workshop on MGD: Report of the Diagnosis Subcommittee (examiners were masked as to final subgroup assignment) [37]. Briefly, subjects were classified based on the Ocular Surface Disease Index (OSDI) and meibum grade scores (MGS) as follows: normal (OSDI<13 and MGS<10), mixed (OSDI≥13 and MGS<10), asymptomatic (Asx) MGD (OSDI<13 and MGS≥10), and MGD (OSDI≥13 and MGS≥10), which has been extensively detailed in three other publications from this work [10, 19, 26].

2.2 System Design and Measurement

The optical system was developed based on a high-resolution optical microscope described elsewhere—a lipid layer microscope (LLM) [3, 35, 38]. The LLM objective lens has a numerical aperture (NA) of 0.6 and a depth of focus (DOF) of ~1.5 μm (58–373, Edmund Optics, New Jersey). A stroboscopic light (X-Strobe 400, Excelitas, Wheeling) serves as the illuminating source. The light has a pulse duration of less than 100 μs, which serves to reduce movement blur of the lipid layer and the eye. Light falling on the cornea at normal incidence is reflected straight back along its incident path. The reflected signal is focused and used to form an image of the ocular surface via a color video camera (acA645-100gc, Basler, Berlin, Germany). The LLM has a circular field of view of 240 μm in diameter and a spatial resolution of 0.56 μm.

All measures were conducted in a dimmed room with controlled temperature (23–25°C) and humidity (30%–50%). The subject's head was positioned on a chin and head rest. After the lipid layer microscopy image was focused on the display, the patient was instructed to gently blink once and to keep their eyes open until they were instructed to close them. The operator used the foot pedal to start data acquisition. After the recording, images that were in focus collected between 4.5 s to 5.0 s after blinking were selected for the analyses described here. The right eye from each subject was imaged with the system twice and averaged. This protocol has been described extensively elsewhere [3, 35].

2.3 Data Analysis

The TFLL thickness was calculated using the interference pattern arising from the lipid layer, as described previously [20, 39]. Briefly, when a TFLL image was acquired with RGB camera, each pixel of the image could be characterized by three values representing the intensity of the three-color channels – red, green, and blue (I_R, I_G, and I_B, respectively). The TFLL thickness of each pixel was determined with the plot of color versus intensity based on the principles of thin film interferometry [3]. To visualize the TFLL distribution over the

surface, shaded surfaces were created using TFLL thickness values for the color data as well as surface height, as shown in Figure 1.

Statistical analyses were conducted using MATLAB (MathWorks, Natick, Massachusetts, USA). The primary outcome of this study was the distribution of TFLL thickness within and across the four disease groups, which were non-normally distributed. The histograms of TFLL thickness were analyzed using a curve-fitting algorithm, as described previously [6]. Probability density functions (PDFs) were fitted to these histograms by a maximum-likelihood method. The Gaussian functions were combined to fit the histograms within each of the four disease groups. A Gaussian distribution is described below:

$$f(\mu,\sigma)=\frac{1}{\sigma\sqrt{2\pi}}e^{-\frac{(x-\mu)^2}{2\sigma^2}} \quad (1)$$

where x represents the TFLL thickness, μ represents the peak of TFLL thickness, and σ represents the standard deviation. A trimodal PDF, including the combination of three Gaussian functions, was created to completely fit the overall profiles as described in equation (2),

$$PDF = p_1 f_1(\mu_1,\sigma_1) + p_2 f_2(\mu_2,\sigma_2) + p_3 f_3(\mu_3,\sigma_3) \quad (2)$$

where p_1, p_2, p_3 are weight fractions (i.e., mixing proportion) of the functions f_1, f_2, f_3 within the PDF, and $p_1 + p_2 + p_3 = 1$. The parameters p_1, p_2, p_3, μ_1, μ_2, μ_3, σ_1, σ_2, σ_3 were adjusted to maximize likelihood. After curve fitting, the distributions of TFLL thickness were summed within the range of standard deviation (σ) away from the mean (μ), i.e., [$\mu\pm\sigma$] according to individual fitted functions f_1, f_2 and f_3.

The goodness of fit for each model was measured using the coefficient of determination (R-square values), ranging from 0 to 1, with those closer to 1 being considered the best fitting. Several models of PDFs were tested to maximize R-squared. Finally, the mixed Gaussian models were chosen to fit the distributions of TFLL thicknesses, yielding R-squared values greater than 0.95 for the trimodal curves for each of the four disease groups. Within a trimodal PDF, p_1, p_2, p_3 are weight fractions (i.e., mixing proportion) of the functions f_1, f_2, f_3. The parameters μ_1, μ_2, μ_3 represent the peaks of TFLL thickness and σ_1, σ_2, σ_3 represent the standard deviations corresponding to the individual three functions. Date are expressed with ± 95% confidence intervals unless otherwise stated.

3 Results

3.1 Subjects

Of the 222 subjects consented, 195 were eligible based on clinical classifications and complete TFLL data were obtained from 190 subjects. Table 1 summarizes the baseline characteristics of these subjects, which has already been described extensively in previous publications [10, 19, 26].

3.2 TFLL Descriptive and Model Parameters from Curve Fitting

The TFLL thickness are summarized in Figure 2. Briefly, two images were obtained from the right eye of each subject. The value of TFLL thickness was first averaged within each image and then averaged between two images. The median value of TFLL thickness in each group was as follows: Normal (67 nm), Mixed (62 nm), Asymptomatic MGD (72 nm), and MGD (60 nm).

Figure 3 illustrates the curve-fitting models of TFLL thickness and Table 3 summarizes the models. From the curve-fitting process, the main outcomes are displayed according to each mode with the position of the peak (μ) and the summed percentage of TFLL thickness values with each mode [$\mu \pm \sigma$]. Note that the percentage is the sum within the range of [$\mu \pm \sigma$] rather than the total range, so the percentage of the three peaks does not add to 100%. The normal group had a distribution with the individual peak position ± 95% confidence intervals and the corresponding summed percentages within each mode as follows: (33.3 ± 0.005 nm, 26%; 53.9 ± 0.019 nm, 40%; 79.4 ± 0.064 nm, 12%). The mixed group had a distribution as follows: 33.8 ± 0.004 nm, 32%; 53.1 ± 0.115 nm, 21%; 71.7 ± 0.232 nm, 27%. The asymptomatic MGD group had a distribution as follows: 33.5 ± 0.004 nm, 20%; 49.2 ± 0.041 nm, 25%; 62.9 ± 0.063 nm, 47%. The MGD group had a distribution as follows: 34.3 ± 0.004 nm, 34%; 53.7 ± 0.022 nm, 28%; 74.9 ± 0.060 nm, 16%. A common mode was observed around 33–34 nm across the four groups, but with different magnitudes of thickness values within these modes. The MGD and mixed groups had the largest percentage of TFLL thicknesses fall within the thinnest modes (peaks 34.3 and 33.8 nm, respectively), particularly compared with the normal and asymptomatic groups. The normal group had the largest percentage of TFLL thickness values fall within mode 2 (peak 53.9 nm), while the asymptomatic MGD group had the largest percentage of TFLL thickness values fall within mode 3 (peak 62.9 nm).

4 Discussion

The aim of this study was to measure TFLL thickness and its variability in the context of MGD. It has been proposed that the TFLL has a uniform multilamellar structure and that TFLL is mainly composed of two parts, a thin monolayer of polar lipids adjacent with the aqueous-mucin gel phase and a thick multilayer lamella of non-polar lipids covering the polar sublayer [40–42]. This study, along with several others, have showed that the TFLL is not uniform under microscopic examination and that a uniform non-polar lipid layer would not be expected to form on the surface of precorneal tear film [3, 13, 18, 35]. This study has also found that the TFLL exhibited unique characteristics across the four disease groups, normal, mixed, asymptomatic MGD, and MGD. This finding reinforces the notion that rough and irregular TFLL surfaces are common in the human tear film structure. Therefore, measures of central tendency when assessing the TFLL, particularly across disease groups, it critically important when probing the data for insight.

The present study showed that there were several obvious peaks in the TFLL distributions across the groups, and that a simple distribution and measures of central tendency do not adequately explain TFLL variation. As shown in Figure 3, the model combined with three-Gaussian functions well-fitted the distributions of TFLL thickness for each of the four

disease groups (R-squares >0.95). The results show that the TFLL contains various modes with different thicknesses and frequencies of observations within those thickness ranges. These results are consistent with a previous study that proposed that localized regions of the TFLL could contain highly thick non-polar lipid aggregates or droplets, whereas other regions were merely a monolayer thick [13]. Therefore, it is possible that the peaks within the histograms of TFLL thickness may correspond to various individual components of the TFLL, i.e., the polar lipid monolayer, non-polar lipid aggregates, or the combination of these components. Further investigations on the TFLL components are required to provide a more detailed clarification for the irregular micrographs of TFLL.

In addition, the recent study showed that both low and high concentrations of polar lipids destabilized the TFLL [13, 43]. Therefore, the ratio between polar and non-polar lipids appears crucial the formation of a TFLL barrier. The findings may, in part, address the controversial relationship between precorneal tear film (PCTF) evaporation rate and TFLL thickness [20, 44–47]. Because a polar lipid monolayer is significantly thinner than the non-polar lipid portion, it is more challenging to capture the subtle alteration of polar lipids in its concentration or its ratio to non-polar lipids. Corroborating this idea, the current study found no significant difference in *overall* (average) thickness across the four groups. However, with the assumption that a monolayer of polar lipids forms the thin areas of TFLL, the thin areas of the TFLL histograms were summed and used the results as the relative percentage of polar lipid monolayer in the TFLL. The percentage thicknesses in each thin mode were 26%, 32%, 20% and 34% in the normal, mixed, asymptomatic MGD, and MGD groups, respectively.

While the concentrations of polar lipids may determine the stability of TFLL, the current study also brought out another property essential to maintenance of a stable TFLL: the thickness gradient across the TFLL micrograph. As shown in Figure 1b, the spatial distribution of TFLL thickness was visualized using a 3D surface plot. There were several regions with steep gradients that are characterized by abrupt changes (e.g., 20 nm to 80 nm, “cliffs”). We propose that these abrupt transitions between “thin” and “thick” regions may be weakly reinforced areas that are easily sheared open under the deformation of the TFLL. It has been demonstrated that the TFLL can withstand shear deformation caused by tangential forces and other extensional deformations [18]. Under the forces of deformation, the stress on the local TFLL region is inversely proportional to its thickness. A greater change in TFLL thickness leads to a greater stress gradient at the local position, and greater susceptibility to disruption via shear forces. Indeed, our previous work has found that the cracks appeared around the edges of thick but not thin TFLL areas [32]. There is also a growing body of evidence to support the idea that the properties of the TFLL in resisting deformation play a key role in the overall stability of the PCTF [48, 49]. A recent study showed that in the context of MGD, different deformation resistance of meibomian secretion was detected between normal and MGD subjects [50]. Further studies quantifying stress gradients across the TFLL is needed to fully understand mechanisms underlying the stability of TFLL *in vivo*.

The novel high-resolution microscopy used herein has permitted a closer examination of the thickness distribution of TFLL in the context of MGD. When combined with contemporary

biochemical techniques to analyze the lipid components of the TFLL and other methods to evaluate the stability of TFLL, the current imaging system may further advance the understanding of role of the TFLL structure and function in health and disease [9, 51].

Acknowledgements:

The authors thank all individuals involved for their contribution in participant recruitment, data collection, and data management for this study in addition to the participants who provided their time to participate in the clinical visit.

5 Financial Disclosures:

Yuqiang Bai: None

William Ngo: William Ngo is an employee of the Centre for Research & Education (CORE). Over the past three years, members of CORE have received funding from the following companies: Alcon, Allergan, Allied Innovations, Brien Holden Vision Institute, CooperVision, GL Chemtec, i-Med Pharma, Johnson & Johnson Vision, Lubris, Menicon, Nature's Way, Novartis, Oté Pharma, PS Therapy, Safilens, Santen, Shire, SightGlass, Visioneering. He has received consulting fees from Alcon.

Safal Khanal: None

Jason J. Nichols: Dr. Jason J. Nichols has received honoraria from Paragon Vision Sciences. He has also received research funding from Alcon, Bruder, Johnson and Johnson Vision, and Mallinckrodt. Kelly Nichols is the spouse of Dr. Jason Nichols, extending her declarations to him. In the past 12 months, Kelly Nichols has consulted for and received honorarium from: Allergan, Aerie, Bruder, Dompe, HanAll Bio, Kala, Novartis, Osmotica, Oyster Point, Sight Sciences, Tear Film Innovations/Alcon, Thea, Tarsus, and TopiVert. Research funding has been received from: Allergan, Kala, and Tear Science.

This work was funded by NIH/NEI R01EY026947, partially supported by NIH/NCATs UL1 TR003096.

References

[1]. Lu H, Wang MR, Wang J, Shen M. Tear film measurement by optical reflectometry technique. J Biomed Opt. 2014;19:027001. [PubMed: 24500519]

[2]. Werkmeister RM, Alex A, Kaya S, Unterhuber A, Hofer B, Riedl J, et al. Measurement of Tear Film Thickness Using Ultrahigh-Resolution Optical Coherence TomographyUltrahigh-Resolution OCT Measurement of Tear Film. Invest Ophthalmol Vis Sci. 2013;54:5578–83. [PubMed: 23847319]

[3]. Bai Y, Ngo W, Nichols JJ. Characterization of the thickness of the tear film lipid layer using high resolution microscopy. Ocul Surf. 2019;17:356–9. [PubMed: 30562612]

[4]. Bai Y, Nichols JJ. In vivo thickness measurement of the lipid layer and the overall tear film by interferometry. Opt Lett. 2019;44:2410–3. [PubMed: 31090693]

[5]. King-Smith PE, Fink BA, Nichols JJ, Nichols KK, Hill RM. Interferometric imaging of the full thickness of the precorneal tear film. J Opt Soc Am A. 2006;23:2097–104.

[6]. Nichols JJ, Mitchell GL, King-Smith PE. Thinning rate of the precorneal and prelens tear films. Invest Ophthalmol Vis Sci. 2005;46:2353–61. [PubMed: 15980222]

[7]. Butovich IA. Tear film lipids. Exp Eye Res. 2013;117:4–27. [PubMed: 23769846]

[8]. Chen J, Green KB, Nichols KK. Characterization of wax esters by electrospray ionization tandem mass spectrometry: double bond effect and unusual product ions. Lipids. 2015;50:821–36. [PubMed: 26178197]

[9]. Chen J, Nichols KK, Wilson L, Barnes S, Nichols JJ. Untargeted lipidomic analysis of human tears: A new approach for quantification of O-acyl-omega hydroxy fatty acids. Ocul Surf. 2019;17:347–55. [PubMed: 30818035]

[10]. Khanal S, Ngo W, Nichols KK, Wilson L, Barnes S, Nichols JJ. Human meibum and tear film derived (o-acyl)-omega-hydroxy fatty acids in meibomian gland dysfunction. Ocul Surf. 2021;21:118–28. [PubMed: 34052415]

[11]. Rantamäki AH, Wiedmer SK, Holopainen JM. Melting points—the key to the anti-evaporative effect of the tear film wax esters. Invest Ophthalmol Vis Sci. 2013;54:5211–7. [PubMed: 23833062]

[12]. Rantamäki AH, Holopainen JM. The effect of phospholipids on tear film lipid layer surface activity. Invest Ophthalmol Vis Sci. 2017;58:149–54. [PubMed: 28114572]

[13]. Paananen RO, Viitaja T, Olżyńska A, Ekholm FS, Moilanen J, Cwiklik L. Interactions of polar lipids with cholesteryl ester multilayers elucidate tear film lipid layer structure. Ocul Surf. 2020;18:545–53. [PubMed: 32562857]

[14]. Bland HC, Moilanen JA, Ekholm FS, Paananen RO. Investigating the role of specific tear film lipids connected to dry eye syndrome: a study on O-Acyl-ω-hydroxy fatty acids and diesters. Langmuir. 2019;35:3545–52. [PubMed: 30712353]

[15]. Cwiklik L Tear film lipid layer: A molecular level view. Biochim Biophys Acta. 2016;1858:2421–30. [PubMed: 26898663]

[16]. Kimball SH, King-Smith PE, Nichols JJ. Evidence for the Major Contribution of Evaporation to Tear Film Thinning between Blinks. Invest Ophthalmol Vis Sci. 2010;51:6294–7. [PubMed: 20688724]

[17]. Nichols JJ, King-Smith PE, Hinel EA, Thangavelu M, Nichols KK. The Use of Fluorescent Quenching in Studying the Contribution of Evaporation to Tear Thinning. Invest Ophthalmol Vis Sci. 2012;53:5426–32. [PubMed: 22789918]

[18]. Georgiev GA, Eftimov P, Yokoi N. Structure-function relationship of tear film lipid layer: A contemporary perspective. Exp Eye Res. 2017;163:17–28. [PubMed: 28950936]

[19]. Bai Y, Ngo W, Khanal S, Nichols KK, Nichols JJ. Human precorneal tear film and lipid layer dynamics in meibomian gland dysfunction. Ocul Surf. 2021;21:250–6. [PubMed: 33771707]

[20]. King-Smith PE, Hinel EA, Nichols JJ. Application of a Novel Interferometric Method to Investigate the Relation between Lipid Layer Thickness and Tear Film Thinning. Invest Ophthalmol Vis Sci. 2010;51:2418–23. [PubMed: 20019370]

[21]. King-Smith PE, Nichols JJ, Nichols KK, Fink BA, Braun RJ. Contributions of evaporation and other mechanisms to tear film thinning and break-up. Optom Vis Sci. 2008;85:623–30. [PubMed: 18677230]

[22]. Parfitt GJ, Xie Y, Geyfman M, Brown DJ, Jester JV. Absence of ductal hyperkeratinization in mouse age-related meibomian gland dysfunction (ARMGD). Aging (Albany NY). 2013;5:825. [PubMed: 24259272]

[23]. Jester JV, Parfitt GJ, Brown DJ. Meibomian gland dysfunction: hyperkeratinization or atrophy? BMC ophthalmology. 2015;15:3–11. [PubMed: 25571963]

[24]. Nelson JD, Shimazaki J, Benitez-del-Castillo JM, Craig JP, McCulley JP, Den S, et al. The international workshop on meibomian gland dysfunction: report of the definition and classification subcommittee. Invest Ophthalmol Vis Sci. 2011;52:1930–7. [PubMed: 21450914]

[25]. Baudouin C, Messmer EM, Aragona P, Geerling G, Akova YA, Benítez-del-Castillo J, et al. Revisiting the vicious circle of dry eye disease: a focus on the pathophysiology of meibomian gland dysfunction. Br J Ophthalmol. 2016;100:300–6. [PubMed: 26781133]

[26]. Khanal S, Bai Y, Ngo W, Nichols KK, Wilson L, Barnes S, et al. Human Meibum and Tear Film Derived (O-Acyl)-Omega-Hydroxy Fatty Acids as Biomarkers of Tear Film Dynamics in Meibomian Gland Dysfunction and Dry Eye Disease. Invest Ophthalmol Vis Sci. 2021;62:13.

[27]. Craig JP, Tomlinson A. Importance of the lipid layer in human tear film stability and evaporation. Optom Vis Sci. 1997;74:8–13. [PubMed: 9148269]

[28]. Isreb M, Greiner J, Korb D, Glonek T, Mody S, Finnemore V, et al. Correlation of lipid layer thickness measurements with fluorescein tear film break-up time and Schirmer's test. Eye. 2003;17:79–83. [PubMed: 12579175]

[29]. Li Y, Lu J, Zhou Q, Wang C, Zeng Q, Chen T, et al. Analysis of clinical and regional distribution characteristics of Obstructive meibomian gland dysfunction in China: A Multicenter Study. Curr Eye Res. 2020;45:1373–9. [PubMed: 32264692]

[30]. Jung JW, Park SY, Kim JS, Kim EK, Seo KY, Kim T-I. Analysis of factors associated with the tear film lipid layer thickness in normal eyes and patients with dry eye syndrome. Invest Ophthalmol Vis Sci. 2016;57:4076–83. [PubMed: 27537256]

[31]. Segev F, Geffen N, Galor A, Cohen Y, Gefen R, Belkin A, et al. Dynamic assessment of the tear film muco-aqueous and lipid layers using a novel tear film imager (TFI). Br J Ophthalmol. 2020;104:136–41. [PubMed: 31000512]

[32]. King-Smith PE, Reuter KS, Braun RJ, Nichols JJ, Nichols KK. Tear Film Breakup and Structure Studied by Simultaneous Video Recording of Fluorescence and Tear Film Lipid Layer Images. Invest Ophthalmol Vis Sci. 2013;54:4900–9. [PubMed: 23766476]

[33]. King-Smith PE, Ramamoorthy P, Braun RJ, Nichols JJ. Tear Film Images and Breakup Analyzed Using Fluorescent Quenching. Invest Ophthalmol Vis Sci. 2013;54:6003–11. [PubMed: 23920365]

[34]. Rantamäki AH, Javanainen M, Vattulainen I, Holopainen JM. Do lipids retard the evaporation of the tear fluid? Invest Ophthalmol Vis Sci. 2012;53:6442–7. [PubMed: 22930719]

[35]. King-Smith PE, Nichols JJ, Braun RJ, Nichols KK. High Resolution Microscopy of the Lipid Layer of the Tear Film. Ocul Surf. 2011;9:197–211. [PubMed: 22023815]

[36]. Lee Y, Hyon JY, Jeon HS. Characteristics of dry eye patients with thick tear film lipid layers evaluated by a LipiView II interferometer. Graefe's Archive for Clinical and Experimental Ophthalmology. 2021;259:1235–41.

[37]. Tomlinson A, Bron AJ, Korb DR, Amano S, Paugh JR, Pearce EI, et al. The International Workshop on Meibomian Gland Dysfunction: Report of the Diagnosis Subcommittee. Invest Ophthalmol Vis Sci. 2011;52:2006–49. [PubMed: 21450918]

[38]. King-Smith PE, Begley CG, Braun RJ. Mechanisms, imaging and structure of tear film breakup. Ocul Surf. 2018;16:4–30. [PubMed: 28935579]

[39]. King-Smith PE, Fink BA, Fogt N. Three Interferometric Methods for Measuring the Thickness of Layers of the Tear Film. Optom Vis Sci. 1999;76:19–32. [PubMed: 10030612]

[40]. Bron AJ, Tiffany JM. The meibomian glands and tear film lipids. Structure, function, and control. Advances in experimental medicine and biology. 1998;438:281–95. [PubMed: 9634898]

[41]. Holly FJ. Formation and rupture of the tear film. Exp Eye Res. 1973;15:515–25. [PubMed: 4712544]

[42]. McCulley JP, Shine W. A compositional based model for the tear film lipid layer. Transactions of the American Ophthalmological Society. 1997;95:79–88; discussion −93. [PubMed: 9440164]

[43]. Suzuki T, Kitazawa K, Cho Y, Yoshida M, Okumura T, Sato A, et al. Alteration in meibum lipid composition and subjective symptoms due to aging and meibomian gland dysfunction. Ocul Surf. 2021.

[44]. Sledge SM, Khimji H, Borchman D, Oliver AL, Michael H, Dennis EK, et al. Evaporation and Hydrocarbon Chain Conformation of Surface Lipid Films. Ocul Surf. 2016;14:447–59. [PubMed: 27395776]

[45]. Fenner BJ, Tong L. More to Stable Tears Than Thickness of the Tear Film Lipid Layer. Invest Ophthalmol Vis Sci. 2015;56:1601. [PubMed: 25745077]

[46]. Finis D, Pischel N, Schrader S, Geerling G. Evaluation of Lipid Layer Thickness Measurement of the Tear Film as a Diagnostic Tool for Meibomian Gland Dysfunction. Cornea. 2013;32:1549–53. [PubMed: 24097185]

[47]. Suzuki S, Goto E, Dogru M, Asano-Kato N, Matsumoto Y, Hara Y, et al. Tear film lipid layer alterations in allergic conjunctivitis. Cornea. 2006;25:277–80. [PubMed: 16633026]

[48]. Rosenfeld L, Fuller GG. Consequences of Interfacial Viscoelasticity on Thin Film Stability. Langmuir. 2012;28:14238–44. [PubMed: 22989061]

[49]. Bhamla MS, Chai C, Rabiah NI, Frostad JM, Fuller GG. Instability and Breakup of Model Tear Films. Invest Ophthalmol Vis Sci. 2016;57:949–58. [PubMed: 26943158]

[50]. Georgiev GA, Yokoi N, Ivanova S, Tonchev V, Nencheva Y, Krastev R. Surface relaxations as a tool to distinguish the dynamic interfacial properties of films formed by normal and diseased meibomian lipids. Soft matter. 2014;10:5579–88. [PubMed: 24959988]

[51]. Panthi S, Chen J, Wilson L, Nichols JJ. Detection of lipid mediators of inflammation in the human tear film. Eye Contact Lens. 2019;45:171–81. [PubMed: 30303825]

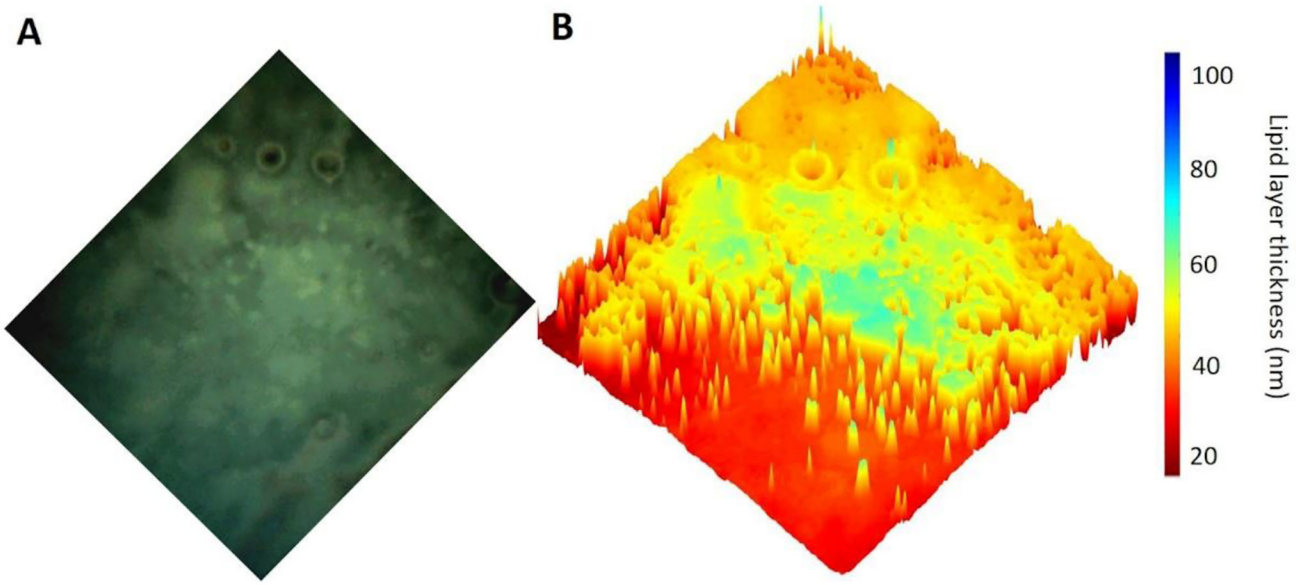

Figure 1.

Quantitative processing of a LLM TFLL image showing physical thickness distribution. (A) Representative image of the TFLL. (B) Visualization of the spatial distribution of TFLL thickness using a 3D surface plot.

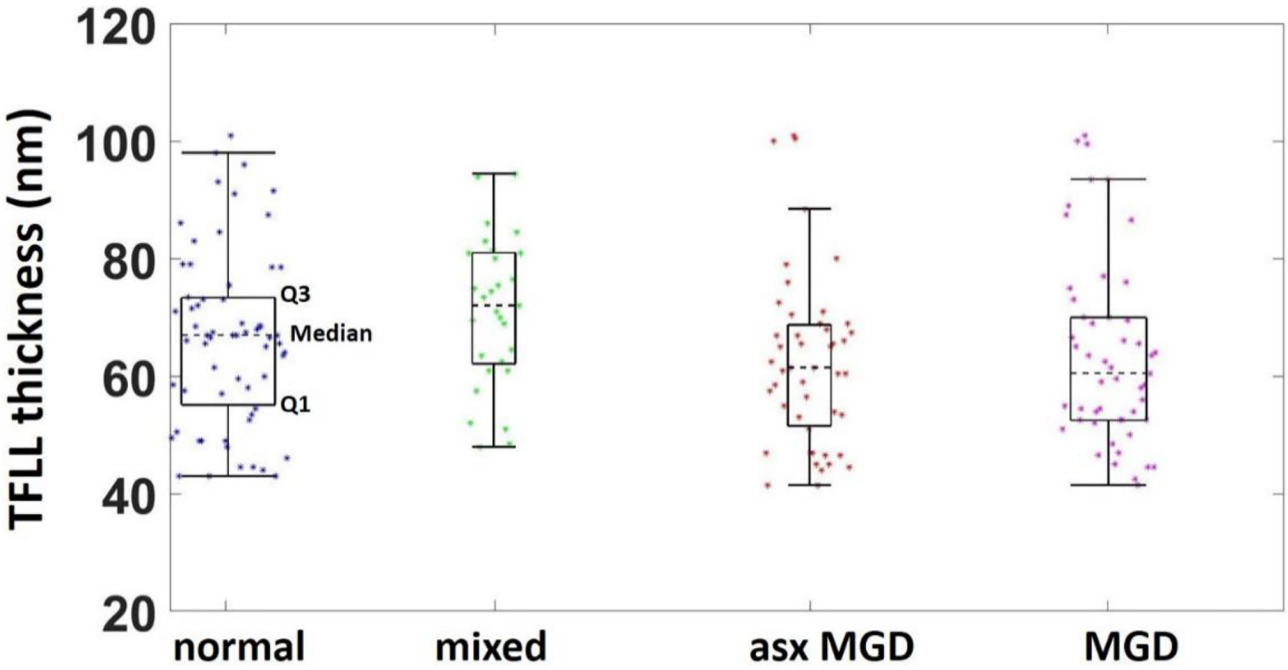

Figure 2.
Summary descriptors of the TFLL thickness by group.

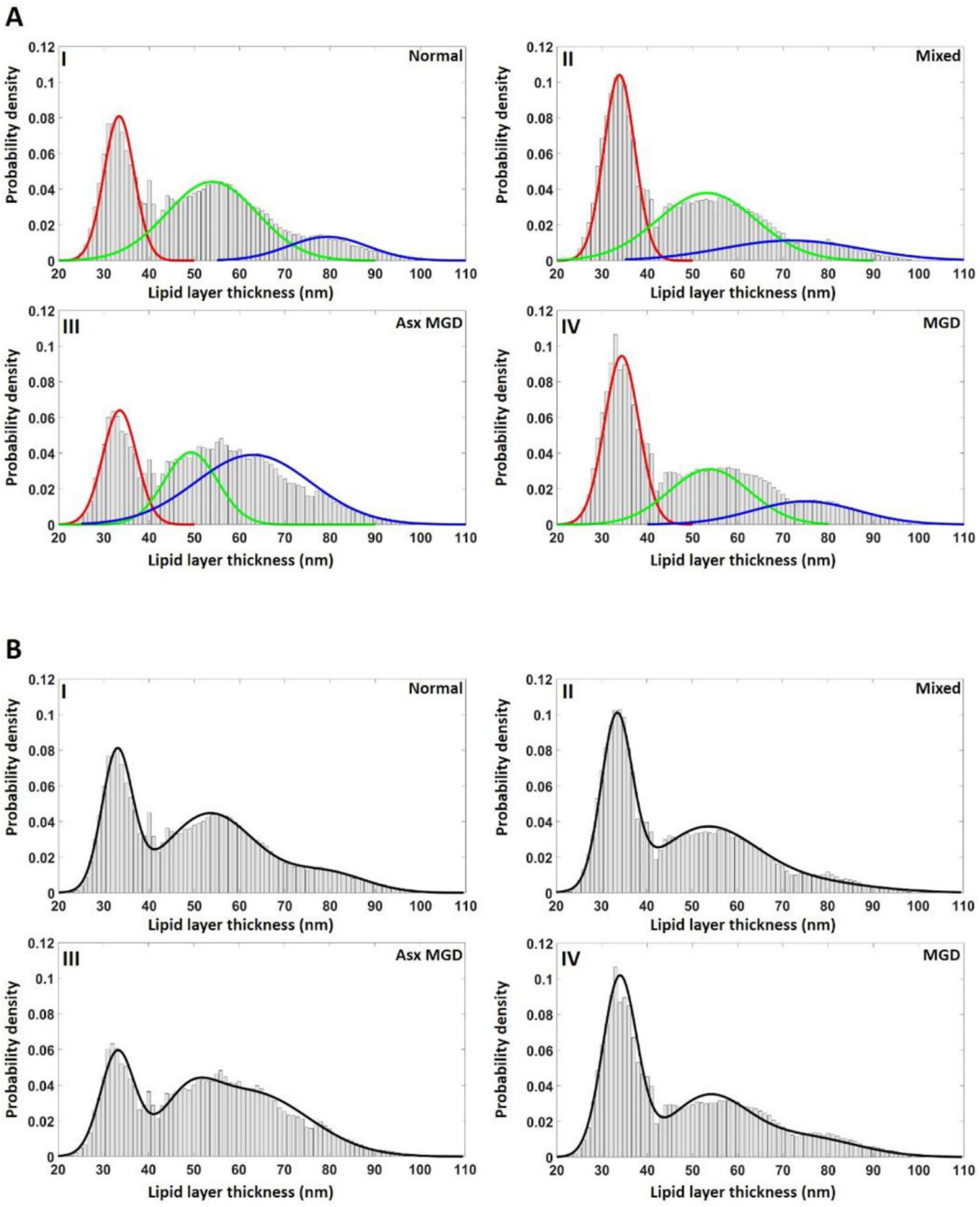

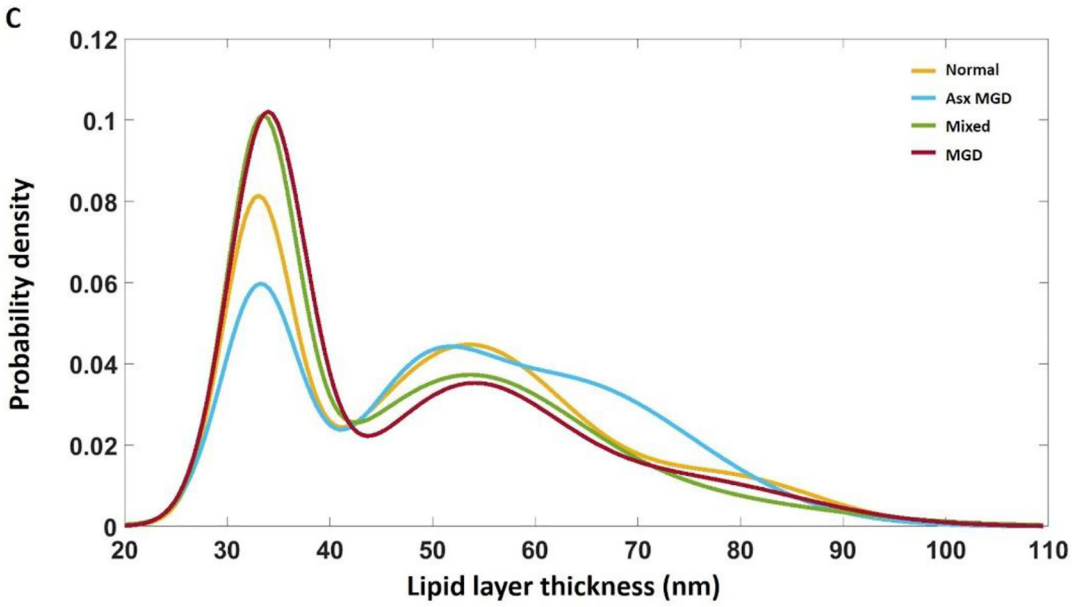

Figure 3.

Histograms and related curve-fitting of the TFLL thickness of the four disease groups. A: Individual Gaussian functions were plotted, overlapping with the histograms of TFLL thickness. B: A trimodal PDF, the sum of three Gaussian functions, was created to completely fit the overall profile of each group. C: The trimodal PDFs for the four disease groups were put together for comparisons. There is a common peak around 33 nm across the four group, but with different magnitudes. Both the mixed and MGD groups exhibit a higher percentage of TFLL thicknesses in thinnest modes compared with the normal and asymptomatic groups.

Table 1:

Baseline characteristics of the study subjects.

	Normal	Mixed	Asymptomatic MGD	MGD
Number of Subjects	63	47	29	51
Male: Female	19: 44	17: 30	12: 17	21: 30
Age Mean ± (SD) years	33.3 ± 13.0	39.7 ± 13.0	38.3 ± 12.5	46.6 ± 14.2
Race (Asian, African Amercian, Causasian, Others)	10, 27, 25, 1	6, 29, 11, 1	3, 13, 13, 0	2, 29, 19, 1

Table 3:

Summary of the TFLL thickness trimodal probability density distributions of the four disease classification groups. p_1, p_2, p_3 are weight fractions (i.e., mixing proportion) of the functions f_1, f_2, f_3. The parameters μ_1, μ_2, μ_3 represent the peak of TFLL thickness and σ_1, σ_2, σ_3 represent the standard deviations corresponding to the three functions.

		Normal	Mixed	Asymptomatic MGD	MGD
R-square		0.96	0.96	0.95	0.97
Function 1	**p 1**	0.32±0.004	0.40±0.001	0.27±0.001	0.47±0.007
	μ 1	33.3±0.005	33.8±0.004	33.5±0.010	34.3±0.004
	σ 1	3.3±0.004	3.4±0.005	3.7±0.008	3.8±0.003
	PCT 1	26%	32%	20%	34%
Function 2	**p 2**	0.56±0.001	0.46±0.003	0.16±0.003	0.37±0.001
	μ 2	53.9±0.019	53.1±0.115	49.2±0.041	53.7±0.022
	σ 2	9.9±0.016	10.8±0.118	5.8±0.042	8.8±0.016
	PCT 2	40%	21%	25%	28%
Function 3	**p 3**	0.13±0.001	0.14±0.004	0.57±0.003	0.17±0.001
	μ 3	79.4±0.064	71.7±0.232	62.9±0.063	74.9±0.060
	σ 3	8.7±0.033	15.2±0.392	12.7±0.021	11.6±0.032
	PCT 3	12%	27%	47%	16%

Note: the percent (PCT) is the sum within the range of [μ ±σ] rather than the total range, so the percentage of the three peaks does not add to 100%.